Appl Magn Reson (2013) 44:619–636
DOI 10.1007/s00723-012-0432-8

Applied
Magnetic Resonance

MRI Comparative Study of Container Geometry Impact on the PMMA Spheres Sedimentation

E. V. Morozov · O. V. Shabanova · O. V. Falaleev

Received: 18 August 2012 / Revised: 22 October 2012 / Published online: 25 January 2013

Abstract Nuclear magnetic resonance (NMR) imaging results are presented for the comparative study of sedimentation of the polymethylmethacrylate colloidal suspensions with spherical particle diameters of 475, 350 and 255 nm. The time evolution of the particle volume fraction in the sedimenting system, velocity of the fluid/suspension interface, interface broadening, and sediment growth velocity are measured against the system concentration as well as the container geometry. Using the experimental data the hindered settling function is evaluated. The influence of the container geometry on the parameters defining the hindered settling function in different approaches is evaluated for the first time. The limiting value of the particle diameter is estimated at which the container geometry has no impact any longer. This effect can be explained by the microscale structure persisting at low Peclet numbers. In addition, the influence of the container geometry on interface broadening and sediment formation for different particle diameters and volume fractions is studied. Spontaneous sediment packing induced by a modified container geometry has been found. NMR imaging has proven to be a highly efficient research tool for studying sedimentation at low Peclet numbers.

1 Introduction

The process of particles falling under the action of gravity through a fluid in which they are suspended, referred to as sedimentation, is attractive for different branches of

E. V. Morozov (✉)
Kirensky Institute of Physics, Siberian Branch of the Russian Academy of Sciences, Akademgorodok 50, 660036 Krasnoyarsk, Russia
e-mail: morozov_if@mail.ru

O. V. Shabanova · O. V. Falaleev
Special Design and Technological Bureau Nauka, Siberian Branch of the Russian Academy of Sciences, Mira st. 53, 660049 Krasnoyarsk, Russia

knowledge. It involves a wide range of problems from life sciences (for example, blood cell settling) to technology (processing of mining fluids containing rock and mineral particles). Therefore, numerous experimental and theoretical investigations of the particle sedimentation in a fluid have been carried out. One of the earliest studies deals with Stokes' analysis of the translation of a single rigid sphere through an unbounded quiescent Newtonian fluid at zero Reynolds number, $Re = \frac{\rho u a}{\mu}$, which led to his well-known law $\mu_0 = \frac{2a^2(\rho_s - \rho)g}{9\mu}$, where u_0 is the settling velocity of an isolated sphere, a is its radius, ρ_s is its density, ρ is the fluid density, μ is the fluid viscosity. Further study was focused on extending Stokes law by considering many-particle case, polydispersity, nonspherical rigid particles, non-Newtonian fluids, and presence of walls, $Re \gg 1$ [1]. At the early stage a major contribution was made by Kynch, Richardson and Zaki, Barnea and Mizrahi [1–6] and others. Today, one of the key questions is whether a sedimenting suspension would be expected to have a random or an ordered microscale structure. It was shown that for low Reynolds numbers and negligible thermal effects, long-range hydrodynamic interactions lead to a highly complex pattern of "swirls" and particle velocity fluctuations [7, 8], i.e., they lead to a microscale structure. Caflisch and Luke were the first to theoretically indicate that the variance of particle velocity fluctuations scales linearly with the size of container [9], but later both the variance limit and average size of swirls for monodisperse spheres were estimated experimentally [10–12]. Finally, correlated regions (swirls) emerging in the system of sedimenting spheres were directly visualized [13].

In the sedimentation studies, the non-Brownian condition is mostly used, i.e., the Brownian forces are negligible compared with the hydrodynamic interaction between the particles. In other words, the dimensionless Peclet number $\mathrm{Pe} = \frac{4/3\pi a^4(\rho_c - \rho)g}{k_B T}$, which measures the relative strength of the hydrodynamic interaction and Brownian forces, is assumed to be infinite. When the gravitational energy gained by a particle sedimenting over a distance of one radius a is equal to the reduced temperature $k_B T$, then $\mathrm{Pe} = 1$, a criterion used to define the start of the colloidal regime. Sedimentation at $\mathrm{Pe} < 1$ has many important applications for colloidal systems, but there are some experimental difficulties caused by a tendency of colloidal particles to form flocks, resulting in complex settling patterns. Nevertheless, one would expect particular colloidal systems to be useful in various applications. So the colloidal suspensions of polymethylmethacrylate (PMMA) spheres with the characteristic diameters of 200–500 nm become extensively introduced into the template synthesis of inverse opals (photonic crystals) [14]. Since the main stage of the template technology is packing of colloidal spheres into a colloidal crystal by means of sedimentation, special attention should be paid to the colloidal suspension of settling spheres in the course of sedimentation process. As mentioned above, the Brownian forces would eliminate any microscale structure appearing in a settling colloidal system [15]. On the contrary, as was theoretically shown, at $\mathrm{Pe} < 1$ the hydrodynamic interaction, though an order of magnitude weaker than the Brownian forces, still induces the backflow effect which is decisive [16]. Thus, whether a sedimenting colloidal suspension could be expected to have an ordered microscale structure is still an open question.

Numerous methods for studying sedimentation have been developed. These are direct measurement, optical methods, light extinction method, X-radiation and ultrasonic adsorption etc. [17]. The concentration profiles, interface displacement

velocity, interface broadening can now be measured for a wide range of both particle volume fractions and particle diameters. It is essential to accurately measure the instantaneous concentration profile of the entire sedimenting suspension in a non-invasive manner. For this purpose the nuclear magnetic resonance (NMR) imaging (MRI) seems to be highly efficient. Using MRI one can track the time evolution of particle volume fraction for the optically opaque systems. To date, the non-Brownian spherical and rod-like particle settling, polydisperse suspension sedimentation and other cases have already been studied by means of MRI [18–20]. First, it is worth noting that the NMR image acquisition time is longer (on the order of several minutes for a general case) than for other express techniques (for instance, Particle Image Velocimetry). It makes the results to be time-averaged, but for a long-time process, this fact can be neglected. Second, for commonly used MRI scanners the image resolution is often limited to ~ 100 μm. Therefore, it is impossible to track the settling particle itself, but if the properties averaged over large volume are interested (for example, dynamics of the interfaces formed in the system during the sedimentation process) this fact can also be neglected.

In our work, MRI is applied to study the sedimentation of the aqueous suspension of non-flocculated monodisperse PMMA spheres (with diameters of 255, 350 and 475 nm). The dynamics of the sedimentation front, its thickness and sediment formation are measured during the sedimentation. In order to reveal whether an ordered microscale structure can originate in sedimenting colloidal suspension, the measurements should be carried out for different characteristic dimensions of the container [13, 21]. But another way to restrict the length scale of the correlated regions is the vertical stratification of the suspension [10, 12]. It is possible to induce the vertical stratification by a special container geometry: in addition to a flat-bottomed vessel, conically and stepwise narrowed vessels were fabricated. It does not prevent the colloidal particles from settling down and packing into a colloidal crystal, but the stratification is generated at a definite height, with the particle volume fraction gradient directed to the bottom. If the microscale structure should originate, it must be strongly affected by the artificially generated stratification. Another advantage of this technique is that it provides an opportunity to find out how a modified container geometry affect the sediment formation dynamics. This is of high importance because the infiltration properties of the colloidal crystal are strongly determined by particles packing in the sediment. Such a problem statement implies that information on (1) the general pattern of colloidal PMMA sphere sedimentation, (2) container geometry impact on the microscale structure, and (3) container geometry impact on the sediment formation is expected to be obtained by means of NMR imaging application.

2 Experimental

2.1 Materials and Methods

Three different batches of colloidal suspensions of PMMA spheres prepared according to a published technique [22] were used. Particle diameters and particle size distribution were measured with an electron microscope. The particle

characteristics, namely, mean diameter $<d>$, ratio of the standard deviation to the mean diameter $\sigma/<d>$, Stokes velocity of an isolated sphere u_s (millimeters per day), Reynolds and Peclet numbers are listed in Table 1. The PMMA particle density is 1.19 g/cm^3, while the density and viscosity of pure water at 25 °C are 1 g/cm^3 and 0.89 mPa s, respectively. Since it was experimentally proved with an electron micrograph that PMMA particles settle under gravity without either aggregation or flock formation, no surfactant addition or other treatment were used.

For sedimentation experiments, three different types of cylindrical fluoroplastic containers were fabricated (Fig. 1): flat-bottomed (F), conically narrowed (C) and stepwise narrowed (S). Every run of the settling experiment started with the same suspension fluid level of 22 ± 1 mm being filled into the vessel. Since settling of the smallest particles of suspension requires more than a month, it is impossible to keep the samples inside the NMR magnet during the entire process. Therefore, the samples were carefully inserted and taken out every time for the image acquisition. Special attention was paid to prevent the samples from shaking and/or tilting. The interface position, velocity and thickness were not influenced by external factors. The experiment was carried out at the room temperature of 25 ± 2 °C. Samples with the different initial concentrations were prepared.

All imaging experiments were carried out using an NMR imaging system based on a Bruker AVANCE DPX 200 ultrashield: magnet with 89 mm diameter vertical bore equipped with self-shielded, water-cooled Bruker gradient set capable of producing maximum gradient strength of 292 mT/m, Bruker radio-frequency (RF) probe PH MINI 0.75, 38 mm internal diameter birdcage coil tuned and matched to the hydrogen (^{1}H) nuclear frequency of 200.13 MHz, with a console operated with Paravision 4.0 software.

The imaging protocol used to acquire two-dimensional (2-D) slice selective MRI images of the sedimenting suspensions was a standard Carr-Purcell-Meiboom-Gill

Table 1 Particle characteristics

Batch	$<d>$, nm	$\sigma/<d>$, %	u_s, mm/d	Re, 10^{-9}	Pe, 10^{-3}
A	475	2.1	2.27	7.0	6.0
B	350	2.9	1.23	2.8	1.8
C	255	2.0	0.66	1.1	0.5

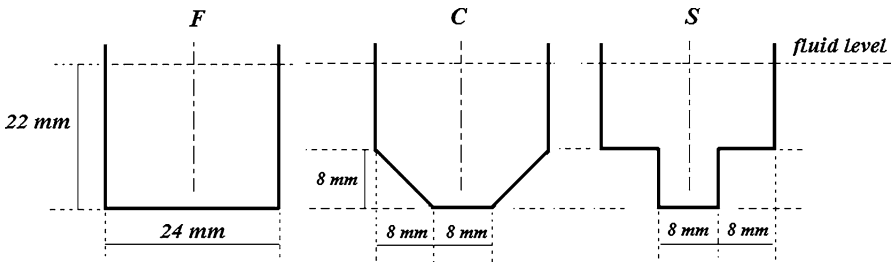

Fig. 1 Different container geometries fabricated for batch sedimentation experiments; flat-bottomed vessel with vertical walls (*F*), conically narrowed vessel (*C*), stepwise narrowed vessel (*S*)

(CPMG) sequence. The proton density (PD)-weighted images and T_2-maps were acquired using Multi Slice Multi Echo (MSME) technique: TR 18 s, TE 4.7 ms, 256 × 256 matrix (128 × 128 for maps), and FOV 40 mm. The T_2-weighted images were acquired using rapid acquisition with relaxation enhancement (RARE) technique: TR 18 s, TE 4.7 ms, with echo train consisting of 64 equally spaced echoes, extending the effective TE to 150 ms, 256 × 256 matrix, and FOV 40 mm.

In sample notation, for example, "F475" the letter F corresponds to the container geometry in Fig. 1 and number 475 denotes the particle diameter listed in Table 1.

2.2 Volume Fraction Calculation

The local concentration of the PMMA particles (referred to as the volume fraction) φ, usually varying in range of $0 < \varphi < 0.6$, plays a key role in the analysis of sedimenting systems. In particular, φ as a function of height h and time t for a suspension is given by [18, 20]:

$$\phi(h,t) = 1 - \frac{S_{\text{susp}}(h,t)}{S_{\text{ref}}}, \tag{1}$$

where $S_{\text{susp}}(h,t)$ and S_{ref} denote the MRI signal intensity for the water protons of suspension and reference sample (for instance, pure water), respectively, along the vertical axis of the container from the fluid level. The MSME technique is used to measure the signal intensity: when PD-weighted images are acquired, the echo signal is generated by a single pair of 90 and 180° RF pulses (as contrasted to the entire echo train used in CPMG technique). As described in earlier works [20, 23], the M_0 value obtained from the mono-exponential analysis of CPMG curves is used to calculate the particle volume fraction to correct for the spin–spin relaxation effects, making it possible to measure φ more accurately.

The analysis of our experimental CPMG curves has shown that the PD-weighted images can be successfully used within the limits of the experimental error. The T_2 values of the PMMA sphere suspensions are sufficiently high (TE/T_2 ratio is <4 % in most cases) to yield a small deviation of the measured signal intensity of clear water and suspension from its actual value which corresponds to M_0. The CPMG curves derived for the region of interest (ROI) placed in clear fluid (water), suspension and sediment are presented in Fig. 2. They are all well described by the equation:

$$S(t) = B + M_0 e^{-\frac{t}{T_2}}, \tag{2}$$

where B is the absolute bias, M_0 is the initial magnetization, T_2 is the spin–spin relaxation time. Moreover, both the mono-exponential character of the experimental curves and the nature of the suspension composed by only monodisperse spheres do not allow the bi-exponential model to be applied for the signal intensity calculation (as it was used for the polydisperse suspension in some works, e.g., [20]). M_0^{susp} and M_0^{sed} values calculated from the mono-exponential analysis yield $\varphi_{\text{susp}} = 0.203$ and $\varphi_{\text{sed}} = 0.515$ for ROI_2 and ROI_3, respectively, which are presented in Fig. 2. On the other hand, the signal intensity of the PD-weighted image yields the volume

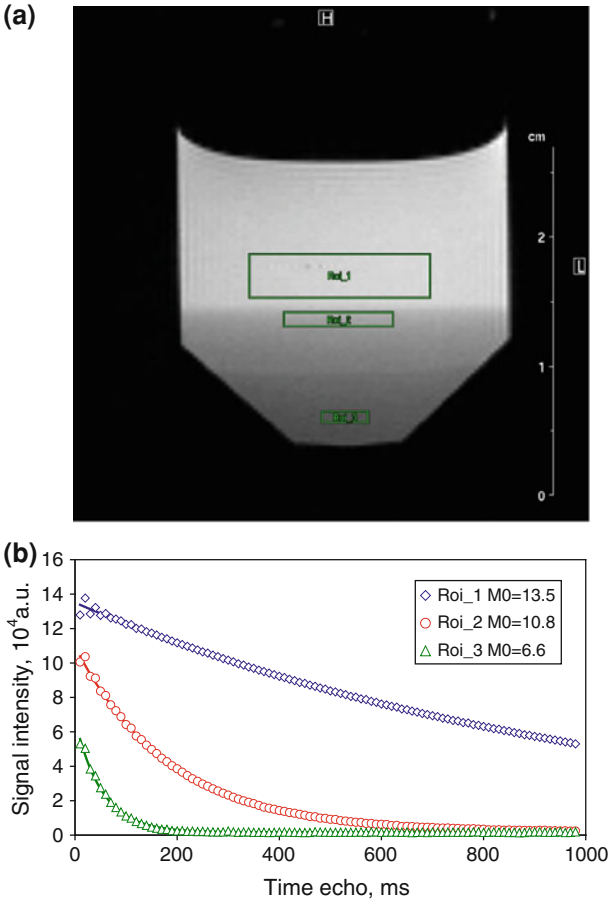

Fig. 2 Image of C350 sample with $\varphi_0 = 7.5$ % (**a**); CPMG experimental curves calculated for ROI highlighted on the image (**b**)

fraction for the suspension and sediment ROI to be 0.206 and 0.546, respectively. The experimental error is equal to about 1.5 % for the suspension and 5.7 % for the sediment volume fraction calculation. Thus, the volume fraction calculated for different samples reveals that the experimental difference between two approaches is usually about 3 %.

2.3 Interface Velocity and Interface Broadening Calculations

Even in a monodisperse system containing spheres of identical size and density, the instantaneous velocities of the individual particles vary about the mean sedimentation velocity. A method was proposed [24, 25] to calculate the average velocity of the diffuse interface, which was found to be within 2 % of the real sedimentation velocity of a monodisperse suspension. The position of the interface was defined by

the location within the clearing front where the total particle volume fraction is equal to one-half of the initial concentration in the bulk suspension:

$$h_{1/2} = h\left(\phi = \frac{\phi_0}{2}\right), \tag{3}$$

where the distance h is measured from the fluid/air interface. In all the cases below, h is measured in the same way. This allows the median interface velocity $u_{1/2}$ to be determined. The value $\varphi = \varphi_0/2$ can be estimated from the volume fraction profile along the container vertical axis. The experiment has shown that the signal intensity profile of T_2-weighted image provides more accurate measurements. It turns out that the sensitivity of T_2-weighted images to changing the volume fraction substantially exceeds the sensitivity of PD-weighted ones. The concentration dependence of T_2 measured for the samples with different initial φ_0 demonstrate the nonlinear but monotonous decrease in T_2 upon increasing the volume fraction. In spite of the nonlinear behavior, the height $h_{1/2}$ on the profiles for both T_2- and PD-weighted images coincides (see Fig. 3, the signal intensity profile of PD-weighted image is fitted to that of T_2-weighted image by linear procedures). This fact allows one to measure the interface more accurately and, thus, the median interface velocity $u_{1/2}$ can be calculated precisely as well, which is essential for dilute samples, where the image contrast is too low to be relied upon.

The displacement of the suspension/sediment interface is measured on the images owing to sufficient contrast provided by any type of weighting. The parameter of quartile fan thickness [24] is not taken into account.

To characterize the time dynamics of the clear fluid/suspension interface thickness, the following quartile interface thickness parameter $\delta(t)$ is usually employed:

$$\delta(t) = h_{1/4}(t) - h_{3/4}(t), \tag{4}$$

where $h_{1/4} = h(\varphi_0/4)$ and $h_{3/4} = h(3\varphi_0/4)$ represent the sedimentation distance of the iso-concentration planes within $\varphi = \varphi_0/4$ and $\varphi = 3\varphi_0/4$, respectively. Because

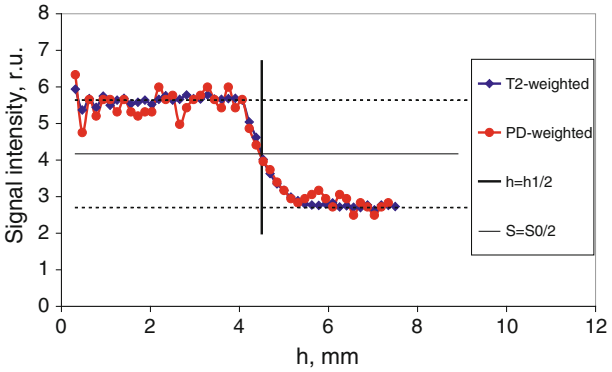

Fig. 3 Signal intensity profiles of T_2- and PD-weighted images along the vertical axis; F350 sample with $\varphi_0 = 20.2$ %

of the insufficient sensitivity of PD-weighted images, use is made of the "full interface thickness" parameter $\delta(t)$, which can be measured more precisely, rather than quartile interface thickness:

$$\delta(t) = h_0(t) - h_1(t), \tag{5}$$

where $h_0 = h(\varphi = 0)$ and $h_1 = h(\varphi_0)$ represent the sedimentation distance of the iso-concentration planes within $\varphi = 0$ (top line of the fluid/suspension interface) and $\varphi = \varphi_0$ (bottom line of the interface), respectively. It has experimentally been found that δ value estimated from the volume fraction profile $\varphi = \mathrm{f}(h)$ is the same as that obtained from the signal intensity profile $S = \mathrm{f}(h)$ of the T_2 weighted image (Fig. 3). Therefore, it is the full interface thickness which is used below.

3 Results and Discussion

3.1 Median Interface Velocity Measurement

The typical volume fraction profiles along the vertical axis in the course of sedimentation are presented in Fig. 4 for different container geometries and different times (days) of settling. In contrast to the flat-bottomed vessel, the linear gradient of the particle volume fraction is originated by conical narrowing from the height where narrowing starts acting till a sediment interface. As can be seen in Fig. 4c, in general, the volume fraction dependence $\varphi = \mathrm{f}(h)$ is not affected by stepwise narrowing (as compared with the flat-bottomed vessel), with the volume fraction profile being only shifted up all over the height of the narrowing impact; in this case the maximum possible value of φ for the narrowed space is found to be achieved very quickly. The influence of narrowing on the sediment formation is discussed below in detail (Sect. 3.3).

Due to the law of mass conservation the area under the profiles (see Fig. 4a) must be constant at different times but it is apparently not the case (0 d and 6 d profiles). This phenomenon can also be found in other works which involve the MRI measurements of volume fraction (e.g., [18]). Higher local volume fractions of the particles in the sediment region are caused by two main factors: losses in the MRI signal intensity and the effect of the short relaxation time T_2 for closely packed media. The losses in the signal intensity are due to the differences in magnetic susceptibility of the particle and the fluid (this phenomenon is comprehensively discussed in Ref. [24]). Moreover, the signal intensity attenuation on the edges of RF coil also contributes to the apparent volume fraction in the sediment region (the latter being usually located close to the coil edge). The effect of the short relaxation time includes the following: the sediment region has a low relaxation time T_2 as compared with the suspension or clear fluid; therefore, the error in the volume fraction calculation is substantial (about 6 % for the CPMG curve presented in Fig. 2b and more than 10 % for some cases) even in case for the smallest TE value which can be used (4.7 ms). As a result, the total volume fraction in the sediment region is overestimated. Moreover, one can find the conservation of area under profiles for times 12, 27 and 45 d against the background of the 6 d profile.

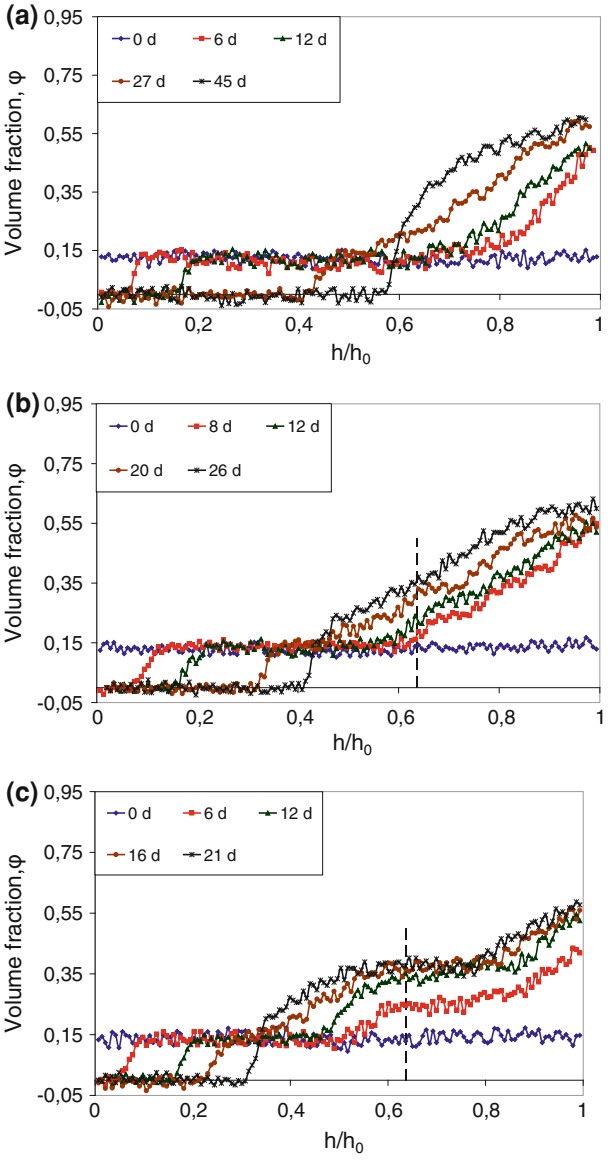

Fig. 4 Time evolution of volume fraction profiles in the process of sedimentation, **a** F350, **b** C350, **c** S350; position of narrowing inset is indicated by *dashed vertical line*

Analyzing the data in Fig. 4, for each geometry type one can find the parts of profiles under the clearing front with the volume fraction equal to their initial values φ_0. The same situation is better observed on the T_2 profiles presented in Fig. 5 for both concentrated and dilute suspensions. The constant value of the volume fraction causes the interface displacement to be linear with time. It allowed the median interface velocity $u_{1/2}$ to be measured in all the samples with different particle batches,

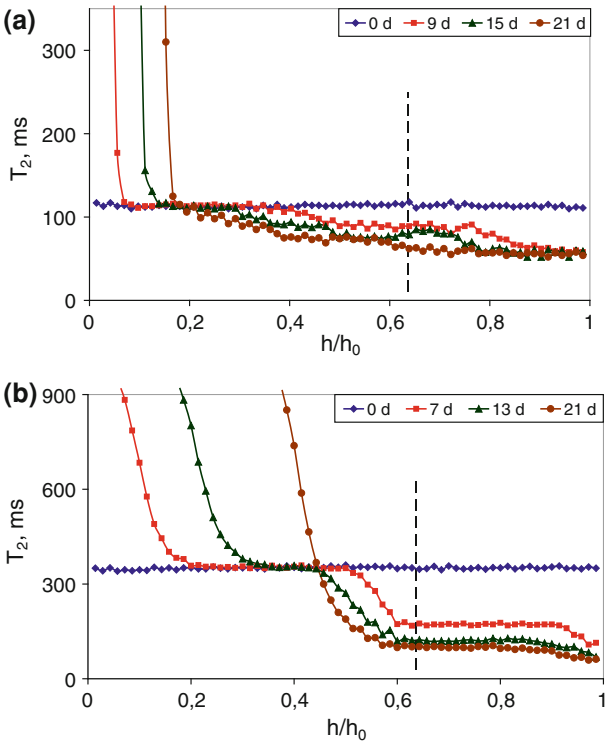

Fig. 5 Time evolution of T_2 profiles in the process of sedimentation, S475 sample with $\varphi_0 = 33.3$ % (**a**), S350 sample with $\varphi_0 = 4$ % (**b**); position of narrowing inset is indicated by *dashed vertical line*

concentrations and container geometries. Based on these data the experimentally determined hindered settling function $f(\varphi) = u_{1/2}/u_s$ against the volume fraction is presented in Fig. 6.

The general behavior of the hindered settling function agrees well with that studied earlier for different sedimenting systems. There are two commonly used approaches to describe the hindered settling function in the volume fraction range of $0.01 < \varphi_0 < 0.4$ which are also employed in this work. Richardson and Zaki [5] first suggested the empirical expression to describe the hindered settling function for non-dilute suspensions, which was slightly modified later [26–28]:

$$f(\phi) = k(1 - \phi)^n, \tag{6}$$

where $n = 5.1$ most accurately represent their data at small Reynolds number and the prefactor k is to be close to 1 (in the range of 0.8–0.9) [15].

The straight line fits well the plot $\ln f(\varphi)$ versus $\ln(1-\varphi)$ and n, k parameters evaluated from these dependences are presented in Table 2. One can see that the value n is affected by the container geometry rather than particle diameter, confirming that the influence of external conditions is higher than the influence of the colloidal suspension features. Garside and Al-Dibouni proposed the following expression for n [27]:

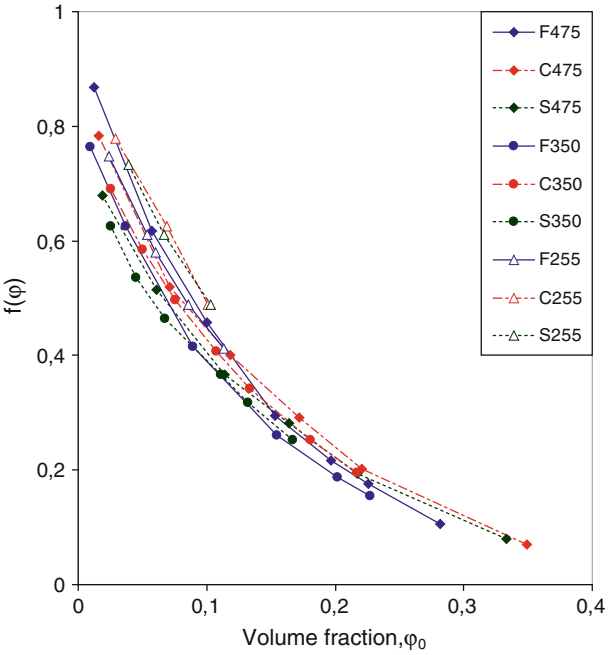

Fig. 6 Hindered settling function versus volume fraction for all the types of samples

Table 2 Parameters n and k for all types of samples

Parameter	F475	C475	S475	F350	C350	S350	F255	C255	S255
n	6.53	5.73	5.50	6.43	5.73	5.67	6.22	6.05	5.86
k	0.91	0.84	0.74	0.79	0.79	0.71	0.86	0.94	0.92

$$\frac{5.1-n}{n-2.7}=0.1Re^{0.9}. \tag{7}$$

Here, the maximum value of n is not expected to be more than 5.1, which is inconsistent with our results. Therefore, further investigations are required.

A more complete expression compared with that described in (6) is the semi-empirical formula obtained by Barnea and Mizrahi [6] which accounts for the role of the average effective hydrostatic pressure gradient of the suspension and the increase of the apparent bulk viscosity of the suspension:

$$f(\phi)=\frac{1-\phi}{(1+T\phi^{1/3})e^{\frac{K\phi}{1-W\phi}}}, \tag{8}$$

where the numerical constants T and W are both found to be equal to 1. The slope of the straight line obtained by plotting $\ln\left[u_{1/2}\left(\frac{1+\varphi^{1/3}}{1-\varphi}\right)\right]$ versus $\varphi/1-\varphi$ allows K to be calculated. The calculated K values are presented in Table 3. It is possible to

Table 3 Parameter K and ratio of $d_{eq}/<d>$ for all types of samples

parameter	F475	C475	S475	F350	C350	S350	F255	C255	S255
K	3.93	3.22	3.06	3.82	3.32	3.2	3.51	3.33	3.28
$d_{eq}/<d>$	1.06	1.02	0.96	0.99	1.00	0.95	1.04	1.08	1.07

compare the equivalent sphere diameter d_{eq} inferred from the value $\ln u_s$ at $\varphi/1-\varphi = 0$ (the y-intercept) with $<d>$ measured directly with an electron microscope (see Table 1). The ratio $d_{eq}/<d>$ is very close to 1 (Table 3), implying that the particles are settling separately and a flock does not appear.

It is obvious that both approaches presented above describe experimental data which are very similar. A simple numerical calculation reveals the relationship between parameters n and K: the hindered settling function numerically calculated by Eq. (8) for the range of K values 1–7 and analyzed in terms of Eq. (6) demonstrates the linear dependence $n = 1.3\ K + 1.5$. Our results (see Tables 2, 3) are very close to this dependence: $n = 1.2\ K + 1.9$, which is within the limits of experimental error.

The experimental results have shown that the properties of colloidal sedimenting systems expressed by means of empirical parameters n and K prove to be highly affected by the container geometry. The results of numerous experiments and calculations clearly show both settling dynamics of non-Brownian particles and variance of particle velocity fluctuations to be influenced by different parameters such as the characteristic length of the container, presence of walls and barriers and stratification (more details can be found in [13] and references therein). This influence is actually due to the impact on the microscale structure formed by the hydrodynamic interaction between particles.

The appearance of large-scale correlated regions was observed experimentally for the particles with Peclet numbers $\mathrm{Pe} \gg 1$ [13, 29, 30]. Some models of emerging correlated regions are described in Refs. [15, 31], including particle volume fraction fluctuations [7, 32]). But in the colloidal regime ($\mathrm{Pe} \leq 1$) the Brownian forces would eliminate any microscale structure appearing in the settling colloidal system. One can see that the descending top interface of settling particles "feels" the environment created by conical and stepwise narrowing in the bottom part of the container. Since no increase (or decrease) in the volume fraction under the interface are observed (volume fraction and T_2 profiles are given in Figs. 4 and 5), the formation of large-scale correlations could explain the experimental impact of the container geometry. Analyzing the data from Tables 2 and 3, one can assume that there is a limiting particle diameter $d_l \sim 140 \div 170$ nm at which the container geometry has no impact any longer (this value being estimated by the linear extrapolation of n, $K = \mathrm{f}(d)$ dependences for all the container geometries). It means that there is a limiting Peclet number when the hydrodynamic particle interaction is completely exceeded by the Brownian motion. This fact is consistent with the evidence obtained in Ref. [16].

MRI alone does not allow one to clarify the mechanism of the container geometry influence on the microscale structure appearing in the colloidal PMMA

sphere suspension. One may suppose the three possible reasons: (1) the backflow caused by narrowing influences the microstructure; (2) restriction of the characteristic length of correlated regions by artificially generated stratification; and (3) increase of the effective surface (i.e., the surface which enables a sediment formation) which plays a key role for the swirl formation (particle packing gives rise to volume fraction fluctuations near the packing front). Since the NMR imaging provides the measurement of only the averaged velocity without any information about its fluctuations, any mechanism is equally possible including overlapping.

3.2 Interface Broadening

As an example, the typical dependences of the total interface thickness on settling time for samples with different initial values of φ_0 are presented in Fig. 7. The main feature of the curves is the presence of the maximum value δ_{max}. It is caused by several effects such as polydispersity, self-sharpening, self-induced hydrodynamic diffusion which might be coupled non-additively. As the initial value of the volume fraction increases, δ_{max} tends to be higher as well as to be shifted to the right-hand side.

To analyze this effect, the dependences of dimensionless $\delta_{max}/\langle d \rangle$ versus φ_0 for the samples with different container geometries are presented in Fig. 8. One can see that the particle diameter decrease as well as the volume fraction increase results in increasing $\delta_{max}/\langle d \rangle$. This is inconsistent with data presented in Ref. [24], where there is an opposite dependence between the interface thickness and volume fraction. This inconsistency is likely to be conditioned by different features of the systems used. In our case, the systems of PMMA spheres are characterized by the narrow size distribution (almost the monodisperse case) coupled with the aggregation stability of the particles themselves. On the contrary, the systems studied in Ref. [24] contain particles with a wide size distribution coupled with the tendency to aggregation and/or flock formation. Therefore, our results disagree with those presented in [24]. Conical and stepwise narrowing, in its turn, influences the ratio $\delta_{max}/\langle d \rangle$; moreover, the suspension of the smallest particles is strongly affected, while this effect is negligible in the suspension of the biggest ones. The experimental behavior observed could

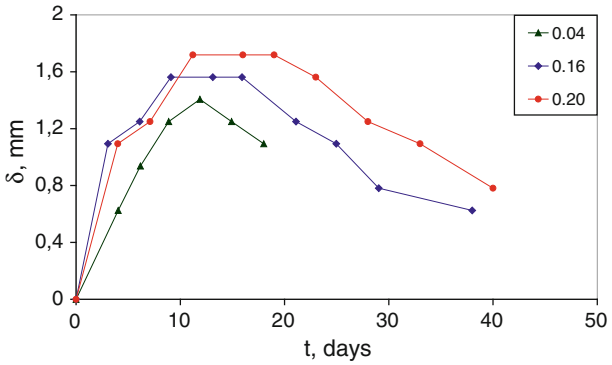

Fig. 7 Dependences of full interface thickness against settling time; F350 sample, initial value of particle volume fraction is indicated

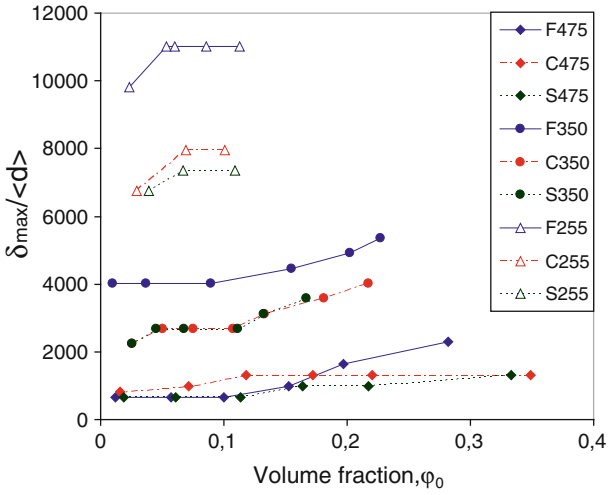

Fig. 8 Dependences of dimensionless $\delta_{max}/<d>$ versus particles volume fraction

have been caused by the reduced time which is necessary for the top interface to reach the bottom one or sediment front (as the particle diameter decreases, the settling time increases substantially). Then, the hindered settling and self-sharpening effects which are more pronounced in the supernatant part of a sedimenting system become involved earlier, resulting in further decrease in δ_{max} as compared with that found for the long time spreading, when the hydrodynamic dispersion has already substantially increased δ_{max}. Thus, it makes no difference which type of narrowing is applied as there is only little difference between conical and stepwise narrowing impact (Fig. 8).

As mentioned above, different effects contribute to the interface thickness. The quartile interface thickness can be expressed as [18, 24]:

$$\delta = \delta_p + \delta_D, \tag{9}$$

where δ_p represents the interface thickness for polydispersity and hindering effects acting alone, and δ_D is the spreading due solely to diffusion. It is assumed that expression (9) can be extended to the full interface thickness instead of the quartile one. It is the case when effects are coupled additively. Davis et al. [24, 25] related the diffusional contribution with the self-induced hydrodynamic diffusivity D_h and the median interface velocity as follows:

$$\delta_D = 1.91\sqrt{\frac{D_h h_{1/2}}{u_{1/2}}}, \tag{10}$$

$$D_h = \frac{du_{1/2}D_h'}{2}, \tag{11}$$

where the effective average diffusivity for the entire surface $D_h^{'}$ depends only on the volume fraction φ. By combining Eq. (9)–(11), it can be written approximately:

$$\frac{\delta - \delta_P}{h_{1/2}} \approx 1.91\sqrt{\frac{D'_h d}{2h_{1/2}}}. \tag{12}$$

If a straight line fits well the plot of $\delta/h_{1/2}$ against $\sqrt{d/2h_{1/2}}$, then the slope corresponds to $1.91\sqrt{D'_h}$. This approach can be applied to the suspensions of non-colloidal spherical particles with diameters up to 3 μm [23, 32]. Our experimental results have shown this approach to be valid for the colloidal PMMA sphere suspension.

As φ_0 increases, the slope becomes more pronounced to result in diffusivity growth. Dependences of the effective average diffusivity D'_h against the initial volume fraction φ_0 for all the sample types are presented in Fig. 9. It is obvious that both particle volume fraction and particle diameter contribute mostly to the increase in D'_h. So, bigger particles exhibit only a weak dependence, while the smaller ones exhibit a strong dependence on increasing volume fraction. It turns out that the container geometry slightly influences D'_h. Unfortunately, NMR imaging does not provide additional information on the origin of such considerable effects. It is only shown in [13] that once the concentration limit is exceeded, the scale of correlated regions emerging in a sedimenting system grows substantially.

3.3 Sediment Formation

It is well known that the settling of the PMMA spheres under gravity is accompanied by crystallization-like packing of particles [14]. In this case, the colloidal crystal formation during sedimentation is usually expected. As a rule, randomly oriented crystals compose the sediment but under special conditions it is possible to prepare a bulk sample of the single colloidal crystal. The container

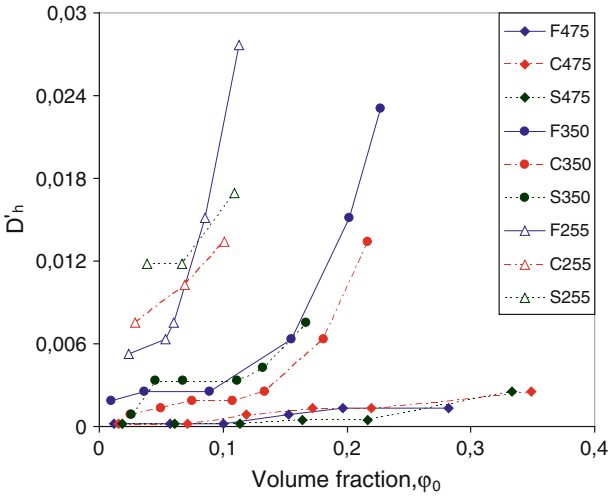

Fig. 9 Dependences of effective average diffusivity versus volume fraction

geometry impact on the sediment formation is studied in terms of the sediment growth velocity and packing fraction.

As mentioned above, the suspension/sediment interface can be visualized very well. It allows the interface displacement to be measured directly from images, and no plotting of the signal intensity profile is required. The dependences of the sediment growth velocity on the initial particle volume fraction are presented in Fig. 10. For the flat-bottomed container, the results are in good agreement with the data calculated in other works according to the mass conservation law $\varphi u = (\varphi^* - \varphi)u^*$, where φ^* is a mean packing fraction and u^* is a sediment growth velocity [13]. But stepwise and conical narrowing substantially accelerate u^* due to the volume fraction enhancement in the supernatant part of the sedimenting system (near the packing front). Changing conditions of the sediment formation in this case allows one to modify the $u^* = f(\varphi_0)$ dependence character as compared with that found for the flat-bottomed container.

The influence of the stepwise narrowed container geometry on the sediment packing has to be described in detail. There is an abnormal behavior of the sediment height during the sedimentation process. Starting with the slow linear dependence the sediment height dramatically grows once a definite moment is reached: one can see a "jump". The effect of spontaneous (avalanche-like) sediment packing can be accounted for by the fact that the maximum available value of φ for the narrowed space is reached very quickly (see the profiles in Fig. 4). As mentioned above (see Sect. 3.1), the stepwise narrowing shifts up the volume fraction profile all over the height of the narrowing impact (in contrast to the conical narrowing which only generates the φ gradient). As the sediment packing front leaves the narrowed space, one can observe the linear behavior found before the jump.

The variation of the sediment growth velocity yields a packing fraction φ^* to be nonuniform along the vertical axis of the container. Consequently, the wave-like

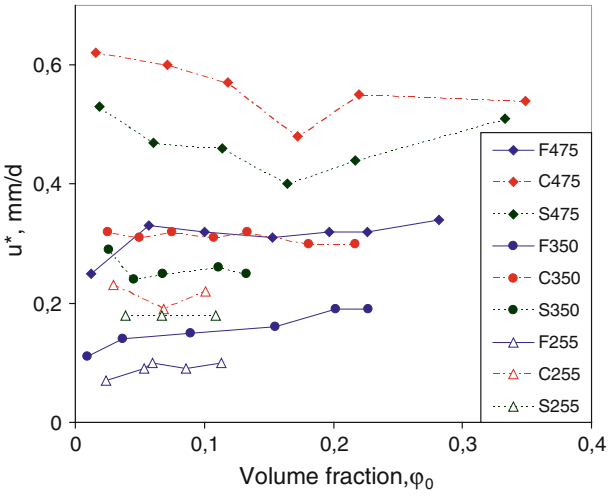

Fig. 10 Dependence of sediment growth velocity versus particle volume fraction

behavior of T_2 along the vertical axis is observed (see Fig. 5a, T_2 profile 15 d), where there is a closely packed region of the suspension above the loosely packed region of the sediment. It is well known [24] that, when lower layers of a compressed sediment makes a fluid to squeeze out, it generates a strong backflow. As a result, the backflow from the narrowed space makes the top layers of the sediment to be rarefied and even lifted up above the entire surface (see Fig. 11a, the black arrow). Other compression consequences manifest in the air bubble formation on the wall (see Fig. 11a, the white arrows) and the surface nucleus formation of closely packed phase on the sediment interface (see Fig. 11b). In this case, the faces of growing colloidal crystal have successfully been visualized by MRI (in Fig. 11c, one can see a coalescence of crystallites formed by narrowing and packed in the top part).

4 Conclusions

In this work, the comparative study of sedimentation of the PMMA colloidal spheres has been carried out using NMR imaging. The evolution of the volume fraction in sedimenting systems with the particle diameters of 475, 350 and 255 nm has been measured non-invasively, making it possible to study the fluid/suspension interface displacement and broadening dynamics. The advantage of the MRI method considerably enlarges the possibilities of the developed experimental techniques for studying colloidal particle sedimentation. So, the median interface velocity, full interface thickness, and sediment growth velocity have been evaluated for different batches of the suspensions, initial volume fractions and settling conditions. It gives us some insight into the mechanism of the processes occurring in the system under study. It turns out that the container geometry influences sufficiently the hindered settling function measured experimentally. Using different semi-empirical approaches this impact is characterized numerically; additionally, the extrapolation of the calculated parameters confirms the existence of the final particle diameter when the container geometry has no impact any longer. This evidences that the microscale structure could persist until the Peclet numbers up to $\sim 10^{-4}$.

The interface broadening is found to depend on the nature of a system rather than on the container geometry: both the maximum achieved value of the full interface

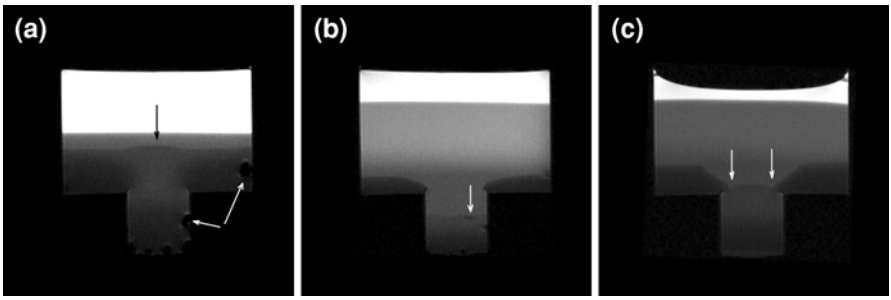

Fig. 11 T_2-weighted images of S475 sample with different $\varphi_0 = 22$ % (**a**, **b**) and $\varphi_0 = 33$ % (**c**) in process of sediment formation

thickness and the effective average diffusivity are mostly affected by the particle diameter. Thus, the effect of the spontaneous (avalanche-like) sediment packing induced by the modified container geometry has been revealed. This effect is of practical importance for the colloidal PMMA crystal growth, making it possible to fabricate specially packed samples.

To conclude, MRI has proved to be highly efficient for the sedimentation study at low Peclet numbers, and this method provides detailed information on the general pattern of the colloidal PMMA sphere sedimentation, container geometry impact on the microscale structure as well as on the sediment formation.

References

1. R. Davis, Ann. Rev. Fluid Mech. **17**, 91 (1985)
2. G.J. Kynch, Trans. Faraday Soc. **48**, 166 (1952)
3. G.K. Batchelor, J. Fluid Mech. **119**, 379 (1982)
4. R. Davis, K.H. Birdsell, AIChE J. **34**(1), 123 (1988)
5. J.F. Richardson, W.N. Zaki, Transact. Inst. Chem. Eng. **32**, 35 (1954)
6. E. Barnea, A. Mizrahi, Chem. Eng. J. **5**, 171 (1973)
7. P.N. Segrè, E. Helbolzheimer, P.M. Chaikin, Phys. Rev. Lett. **79**, 2574 (1997)
8. D.L. Koch, E.S.G. Shaqfeh, J. Fluid Mech. **224**, 275 (1991)
9. R.E. Caflisch, J.H.C. Luke, Phys. Fluids **28**, 759 (1985)
10. S.Y. Tee, P.J. Mucha, L. Cipelletti, S. Manley, M.P. Brenner, P.N. Segré, D.A. Weitz, Phys. Rev. Lett. **89**, 054501 (2002)
11. L. Bergougnoux, S. Ghicini, E. Guazzelli, J.E. Hinch, Phys. Fluids **15**, 1875 (2003)
12. D.C. Gómez, L. Bergougnoux, E.J. Hinch, E. Guazzelli, Phys. Fluids **19**, 098102 (2007)
13. P. Snabre, B. Pouligny, C. Metayer, F. Nadal, Rheol. Acta **48**, 855 (2009)
14. G.I.N. Waterhouse, M.R. Waterland, Polyhedron **26**, 356 (2007)
15. Y. Xiaolong, D.L. Koch, Phys. Fluids **19**, 093302 (2007)
16. J.T. Padding, A.A. Louis, Phys. Rev. Lett. **93**, 220601 (2004)
17. R.A. Williams, C.G. Xie, R. Bragg, W.P.K. Amarasinghe, Colloids Surf. **43**, 1 (1990)
18. M.A. Turney, M.K. Cheung, M.J. McCarthy, R.L. Powell, Phys. Fluids **7**(5), 904 (1995)
19. M.K. Cheung, R.L. Powell, M.J. McCarthy, AIChE J. **42**(1), 271 (1996)
20. J. Acosta-Cabronero, L.D. Hall, AIChE J. **55**(6), 1426 (2009)
21. H. Nicolai, E. Guazzelli, Phys. Fluids **7**(1), 3 (1995)
22. R.C. Schroden, M. Al-Daous, C.F. Blanford, A. Stein, Chem. Mater. **14**, 3305 (2002)
23. M.A. Turney, M.K. Cheung, R.L. Powell, M.J. McCarthy, AIChE J. **41**, 251 (1995)
24. J. Acosta-Cabronero, Ph.D. thesis, University of Cambridge, Cambridge, 2006
25. R.H. Davis, M.A. Hassen, J. Fluid Mech. **196**, 107 (1988)
26. R. Di Felice, Int. J. Multiphase Flow **25**, 559 (1999)
27. J. Garside, M.R. Al-Dibouni, Ind. Eng. Chem. Process Des. Dev. **16**, 206 (1977)
28. R. Davis, K.H. Birdsell, AIChE J. **34**, 123 (1988)
29. E. Guazzelli, Phys. Fluids **13**, 1537 (2001)
30. P.N. Segré, Phys. Rev. Lett. **89**, 254503 (2002)
31. P. Boogerd, B. Scarlett, R. Brower, Irrig. Drain. **50**, 109 (2001)
32. J.M. Ham, G.M. Homsy, Int. J. Multiphase Flow **14**(5), 533 (1988)